

# Fe II/Mg II Emission Line Ratio in High Redshift Quasars \*

M. Dietrich <sup>1,2</sup>, F. Hamann <sup>1</sup>, I. Appenzeller <sup>3</sup>, and M. Vestergaard <sup>4</sup>  
*dietrich@chara.gsu.edu*

## ABSTRACT

We present results of the analysis of near infrared spectroscopic observations of 6 high-redshift quasars ( $z \gtrsim 4$ ), emphasizing the measurement of the ultraviolet Fe II/ Mg II emission line strength in order to estimate the beginning of intense star formation in the early universe. To investigate the evolution of the Fe II/Mg II ratio over a wider range in cosmic time, we measured this ratio for composite quasar spectra which cover a redshift range of  $0 \lesssim z \lesssim 5$  with nearly constant luminosity, as well as for those which span  $\sim 6$  orders of magnitude in luminosity. A detailed comparison of the high-redshift quasar spectra with those of low-redshift quasars with comparable luminosity shows essentially the same Fe II/Mg II emission ratios and very similar continuum and line spectral properties, i.e. a lack of evolution of the relative iron to magnesium abundance of the gas in bright quasars since  $z \simeq 5$ . Current nucleosynthesis and stellar evolution models predict that  $\alpha$ -elements like magnesium are produced in massive stars ending in type II SNe, while iron is formed predominantly in SNe of type Ia with intermediate mass progenitors. This results in an iron enrichment delay of  $\sim 0.2$  to  $0.6$  Gyr. We conclude that intense star formation activity in the host galaxies of  $z \gtrsim 4$  quasars must have started already at an epoch corresponding to  $z_f \simeq 6 - 9$ , when the age of the universe was  $\sim 0.5$  Gyr ( $H_0 = 72 \text{ km s}^{-1} \text{ Mpc}^{-1}$ ,  $\Omega_M = 0.3$ ,  $\Omega_\Lambda = 0.7$ ). This epoch corresponds well to the re-ionization era of the universe.

*Subject headings:* galaxies: quasars — galaxies: high-redshift — galaxies: Fe II emission — galaxies: elemental abundance

## 1. Introduction

There is growing evidence that galaxy formation and intense star formation are closely related to quasar activity, particularly in the early universe. For example, the detections of large amounts of molecular gas and dust ( $M_{\text{molec.}} \simeq 10^{10} M_\odot$ ,  $M_{\text{dust}} \simeq 5 \times 10^8 M_\odot$ ) around quasars

at redshifts  $z \gtrsim 4$  (Isaak et al. 1994; Ohta et al. 1996; Andreani et al. 1999; Carilli et al. 2000, 2002; Omont et al. 1996, 2001) establish a close relationship between quasars and massive galaxies. There is also solid evidence that the co-moving space density of quasars and the cosmic star formation rate both show a strong increase toward higher redshifts (Lilly et al. 1996; Connolly et al. 1997; Tresse & Maddox 1998; Steidel et al. 1999; Lanzetta et al. 2002). At low redshifts it has been found that characteristic physical properties of quasar host galaxies, e.g., bulge mass, luminosity and stellar velocity dispersion, are well correlated with the mass of the central black hole (Kormendy & Richstone 1995; Gebhardt et al. 2000; Merritt & Ferrarese 2001; Ferrarese & Merritt 2001; Tremaine et al. 2002). Moreover, it has become clear that all massive galaxies today harbor super massive black holes (SMBHs) in their centers, implying that at one time (early in their

<sup>1</sup>Department of Astronomy, University of Florida, 211 Bryant Space Science Center, Gainesville, FL 32611-2055, USA

<sup>2</sup>Department of Physics & Astronomy, Georgia State University, One Park Place South SE, Suite 700, Atlanta, GA 30303, USA

<sup>3</sup>Landessternwarte Heidelberg-Königstuhl, Königstuhl 12, D-69117 Heidelberg, Germany

<sup>4</sup>Department of Astronomy, The Ohio State University, 140 West 18th Av., Columbus, OH 43210-1173, USA

\* Based on observations collected at the CTIO Observatory, Chile, at the European Southern Observatory, Paranal, Chile, and the the W.M. Keck Observatory, Hawai'i

evolution) these galaxies were hosts to active, i.e. quasar or quasar-like, nuclei.

Since quasars are among the most luminous objects in the universe they can be observed at practically any distance at which these objects occur. This practical aspect together with their close relation to galaxy and star formation history makes quasars excellent probes to study these processes in the early universe. Assuming that the gas of the broad emission line region (BELR) originates from the interstellar medium of the quasar host galaxies, these lines provide valuable information on the chemical composition and enrichment history of the quasar host galaxies. Analysis of ultraviolet broad emission lines (BELs), as well as intrinsic associated absorption lines in quasar spectra, indicate that the gas-phase metallicities near quasars are at least solar to several times solar at even the highest measured redshifts (e.g., Hamann & Ferland 1992, 1993, 1999; Ferland et al. 1996; Korista et al. 1996; Hamann 1997; Dietrich et al. 1999; Pettini 1999; Dietrich & Wilhelm-Erkens 2000; Warner et al. 2002; Dietrich et al. 2003a,b). These results show that well before the epoch corresponding to  $z \simeq 3$  to 4 significant star formation must have taken place in the galactic or proto-galactic cores where these quasars reside (e.g., Cen & Ostriker 1999) to enrich the gas phase.

The epoch of first intense star formation activity in quasar host galaxies can also be dated exploring the abundance of  $\alpha$ -process elements relative to iron. According to present chemical enrichment scenarios,  $\alpha$ -element nuclei are produced predominantly in type II SNe with massive progenitors on time scales of  $\tau_{evol} \simeq 2 - 10$  Myr. On the other hand, the dominant source of iron is assumed to be type Ia SNe at the end point of the evolution of intermediate mass stars in binary systems, about  $\tau_{evol} \simeq 1$  Gyr after the onset of the star formation epoch (e.g., Tinsley 1979; Matteucci & Greggio 1986; Wheeler et al. 1989; Yoshii et al. 1996). The amount of iron returned to the interstellar medium in SNII ejecta is rather low (Yoshii et al. 1996, 1998). It is generally assumed that the significantly different time scales of the release of  $\alpha$ -elements and iron to the interstellar medium results in a time delay of the order of  $\sim 1$  Gyr in the iron enrichment. However, recent studies by Matteucci (1994), Friaça & Terlevich (1998), and Matteucci & Recchi (2001) indicate

that this delay may be  $\sim 0.2 - 0.6$  Gyr for elliptical galaxies. Detecting Fe II emission at high redshift comparable to the relative strength observed in quasars at lower redshift indicates that the formation of the stars which had released the iron had occurred  $\sim 0.3 - 0.8$  Gyr earlier in the quasar host galaxy. Therefore, the line ratio of  $\alpha$ -element vs. iron emission can be used as a cosmological clock (e.g., Hamann & Ferland 1999; Matteucci & Recchi 2001).

A suitable spectral feature for representing the presence of  $\alpha$ -elements is the prominent Mg II resonance doublet at  $\lambda\lambda 2795, 2803$  Å (hereafter Mg II $\lambda 2798$ ). The generally strong UV Fe II multiplets around Mg II in quasar spectra ( $\lambda\lambda \sim 2000 - 3000$  Å; Wills et al. 1980; Grandi 1981; Netzer et al. 1985), are probably the most promising for obtaining at least some information on the relative iron abundance (e.g., Wampler & Oke 1967; Wills et al. 1985; Hamann & Ferland 1999). Since Mg $^+$  and Fe $^+$  have similar ionization potentials (7.6 eV and 7.9 eV, respectively), it is generally assumed that Mg II $\lambda 2798$  and the Fe II emission both originate in the partially ionized zone of the line emitting gas. However, it is important to keep in mind that the Mg II $\lambda 2798$  and Fe II emission are differently affected by the conditions of the line emitting gas. As Wills et al. (1985) pointed out, the Fe $^+$  zone is much more extended than Mg $^+$  zone and contains hot regions where magnesium is ionized to Mg $^{++}$ , which emits Mg II much less efficiently. Furthermore, Mg II $\lambda 2798$  and the Fe II emission show significantly different radiative transfer properties. While Mg II $\lambda 2798$  is a pair of two resonance lines Fe II involves several ten thousand lines. Due to these thousands of transitions, Fe II is subject to processes like line fluorescence, Ly $\alpha$  pumping and turbulence (e.g., Verner et al. 1999) which results in a complicated line transfer. It is also known that UV Fe II emission suffers destruction by Balmer continuum absorption and conversion to optical Fe II emission for large column densities,  $N_H \gtrsim 10^{24}$  cm $^{-2}$ , (Wills et al. 1985; Joly 1987). Since Mg II $\lambda 2798$  forms predominantly in regions of higher Balmer continuum opacity and these lines are closer to the wavelength of the Balmer edge than the strong UV Fe II emission, Mg II $\lambda 2798$  emission is more reduced than UV Fe II by Balmer continuum absorption (Wills et al. 1985). Another process which affects

the Fe II and Mg II $\lambda 2798$  emission are charge exchange reactions. As pointed out by Joly (1987) for  $T_e \gtrsim 10^4$  K Fe $^+$  is ionized to Fe $^{++}$  by charge exchange reactions while Mg $^+$  is nearly unaffected by this process. Given the complexity of the Fe II emission spectrum accurate iron abundances are not yet straight forward to deduce and a full synthesis of individual quasar spectra is required. This seriously complicates such measurements because the Fe II emission is hard to synthesize (e.g., Verner et al. 1999; Collin & Joly 2000; Sigut & Pradhan 1998, 2003).

However, in spite of these uncertainties which affect the Fe II and the Mg II $\lambda 2798$  line emission, the Fe II/Mg II emission ratio also must reflect the Fe/Mg abundance. While, in view of the uncertainties concerning the detailed physical processes, it may not be possible to derive absolute abundances from these lines, it should, nevertheless, be possible to derive at least variations of the Fe/Mg ratio with redshift from emission line ratios if objects with similar observed physical properties are compared. This is feasible owing to the similar appearance of their optical-UV spectra across the known redshift and luminosity ranges (Dietrich et al. 2002b) and the observed similar variability properties (Peterson & Wandel 1999, 2000; Onken & Peterson 2002), suggesting a generally similar physical structure of the AGN emission-line regions. Assuming that the physical conditions of the line emitting gas are comparable for different objects, the effects mentioned above should influence the Fe II/Mg II $\lambda 2798$  line ratio measured in individual quasars in a very similar way. To minimize the uncertainties that are introduced by, for example, different radiative transfer properties and different conditions of the line emitting gas ( $T_e, N_H, n_e$ ), we concentrate (a) on individual quasars of similar intrinsic luminosity and (b) on composite quasar spectra of comparable luminosity as the individual high redshift quasars. This approach, adopted in this work, reduces the influence of a possibly luminosity dependent spectral energy distribution (SED) of the incident ionizing continuum on the physical conditions of the line emitting region. As a consequence, similar continua will result in similar conditions of the line emitting gas, emphasizing effects of relative abundance variations. Assuming that the physical parameters affecting Fe II/Mg II are roughly

the same at all redshifts, then the average of measured Fe II/Mg II ratios at different redshifts will yield useful constraints on the redshift evolution of Fe/Mg.

Observations of the Mg II $\lambda 2798$  and of the rest-frame UV-multiplets of Fe II in the spectra of several high-redshift quasars have been published by Hill et al. (1993), Elston et al. (1994), Kawara et al. (1996), Taniguchi et al. (1997), Murayama et al. (1998, 1999), Yoshii et al. (1998), Thompson et al. (1999), Green et al. (2001), Dietrich et al. (2002a), Iwamuro et al. (2002), and Freudling et al. (2003). Generally, fairly strong Fe II emission was found, indicating a very early cosmic epoch of the first star formation in the high-redshift quasar host galaxies.

In order to obtain more quantitative information on the beginning of the first star formation episode in quasar host galaxies at high redshifts, we extend our study of 6 high-redshift quasars  $z \simeq 3.4$  (Dietrich et al. 2002a) to earlier cosmic epochs. We observed 6 quasars with redshifts  $4.4 \lesssim z \lesssim 5$  to extend the redshift range and increase the sample size. This high redshift range corresponds a time when the universe was less than  $\sim 1.3$  Gyr old ( $H_o = 72 \text{ km s}^{-1} \text{ Mpc}^{-1}$ ,  $\Omega_M = 0.3$ ,  $\Omega_\Lambda = 0.7$ ; Carroll et al. 1992; Freedman et al. 2001). To put this study on the evolution of the Fe II/Mg II ratio at high redshifts in a wider cosmological context, we analyzed quasar composite spectra which we calculated for a wide range in luminosity ( $\sim 6$  orders of magnitude) and redshift ( $0 \lesssim z \lesssim 5$ ) to study continuum and emission line correlations, i.e. the Baldwin-Effect (Dietrich et al. 2002b).

We find a lack of evolution of the measured Fe II/Mg II emission line ratios in these high-redshift quasars compared to those in quasar spectra at low-redshifts. This indicates that the relative iron to magnesium abundance of the gas in bright quasars is unchanged since  $z \simeq 5$ . We conclude that intense star formation activity in the host galaxies of the studied high-redshift quasars must have started already at an epoch corresponding to  $z_f \simeq 6 - 9$ , when the age of the universe was  $\sim 0.5$  Gyr. This epoch corresponds well to the re-ionization era of the universe.

## 2. Observations and Data Analysis

We observed 6 quasars with redshifts  $4.4 \lesssim z \lesssim 5.0$  to measure the Fe II/Mg II ratio in the restframe ultraviolet (hereafter referred to as the  $z = 4.5$  sample). The spectra were recorded using infrared spectrographs of the W.M. Keck Observatory at Hawai'i, the Cerro Tololo Inter-American Observatory (CTIO) at Chile, and the ESO VLT Paranal Observatory at Chile (Table 1). The quasars were selected to be accessible at the time of observation and to be bright enough to be observed within reasonable integration times. Furthermore, UV emission lines like C IV  $\lambda 1549$  are uncontaminated by strong and broad absorption features. For the selected redshifts the prominent Mg II  $\lambda 2798$  emission line and most of the strong ultraviolet Fe II emission at  $\lambda \lambda 2300 - 2600 \text{ \AA}$  are redshifted into the near infrared H-band. We covered practically the whole restframe wavelength range  $\lambda \lambda 2200 - 4500 \text{ \AA}$  continuously, which made it possible to derive reliable continuum fits and, thus, at least internally accurate flux values for the ultraviolet Fe II emission. In addition to the  $z \gtrsim 4.4$  quasars, Q 2050–358 ( $z = 3.5$ ) was recorded to enlarge our sample of quasars at  $z \simeq 3.4$  (hereafter ‘the  $z = 3.4$  sample’). The details of the data aquisition and processing are described in the following subsections.

### 2.1. Keck II NIRSPEC Observations

The high redshift quasar PC 1158+4635 ( $z=4.733$ ; Schneider et al. 1989) was observed in service mode with NIRSPEC at KECK II in the near infrared domain on May 19/20, 2000. The seeing was  $\sim 0''.5$ , estimated from the spatial profile of the standard star spectra. The  $1024 \times 1024$  InSb detector array was used in the longslit mode ( $0''.76 \times 42'', 0''.19/\text{pixel}$ ). To cover the near infrared spectral range three settings of the grating were used which yield the wavelength ranges  $(1.26 - 1.54)\mu\text{m}$ ,  $(1.52 - 1.81)\mu\text{m}$ , and  $(2.05 - 2.48)\mu\text{m}$  which cover the traditional J, H, and K bands, respectively. Making use of the slit length the location of the object along the slit was alternated by  $\sim 20''$  for subsequent exposures to assure a proper sky-correction. Due to the high brightness of the night sky in the near infrared, the integration times of the individual exposures of the quasar were limited to 120 sec and 400 sec,

respectively. The observation log and the total integration times for the individual bands are given in Table 1.

A mean dark frame was calculated using 5 individual dark frames. Flatfield frames were taken in the lamp-on and lamp-off mode for each wavelength range. The frames corrected for thermal background were used to compute normalized flatfield frames for the flatfield correction (Horne 1986). Argon comparison spectra were recorded for wavelength calibration for each wavelength range. In the J to H infrared wavelength range the spectral resolution, measured using the FWHM of strong night sky emission lines, amounts to  $R = 570$  corresponding to  $\Delta v \simeq 520 \text{ km s}^{-1}$  and in the K wavelength range it amounts to  $R = 650$  ( $\Delta v \simeq 460 \text{ km s}^{-1}$ ). Because the sky brightness can vary significantly on time scales of minutes (comparable to our exposure times) we used the sky spectrum measured along the slit in each frame to subtract the sky emission. A 3<sup>rd</sup> to 6<sup>th</sup> order polynomial fit was calculated for each wavelength element to describe the spatial intensity distribution of the night sky emission. The fit based on  $\sim 18''$  wide regions which were  $\sim 5''$  separated from quasar or standard star.

The standard star HD 105601 ( $m_K = 6.685$ , A2V; Elias et al. 1982; Arnaud et al. 1989) was observed for each setting before or after the observations of the quasar spectrum for flux calibration and correction of the strong atmospheric absorption features. To obtain a sensitivity function we assumed that the spectral energy distribution of HD 105601 can be described in the near infrared wavelength range with a black body spectrum. We applied  $T_{\text{eff}} = 8995 \text{ K}$  to computed a black body spectrum for the observed wavelength range. This black body spectrum was scaled to match the apparent magnitudes of HD 105601 in the J-, H-, and K-band (Elias et al. 1982).

We used the spatial curvature of the standard star spectrum to trace the location of the slightly curved quasar spectrum. The spectra of the individual exposures were extracted using an optimal extraction routine (Horne 1986).

The 1 D quasar spectra were corrected for broad atmospheric absorption bands using an appropriately scaled transmission function derived from HD 105601. Cosmic-ray events in the individual 1 D spectra were corrected by comparing the

spectra with each other. Finally, we computed a weighted mean of the quasar spectra for each setting, with the weight given by the signal-to-noise ratio of the continuum. These mean quasar spectra were flux calibrated using the corresponding sensitivity function for the wavelength range. The mean spectra of each setting were rebinned to a uniform stepsize in wavelength and merged. The flux calibrated spectrum of PC1158+4635 is shown in Figure 1.

## 2.2. CTIO Observations

On Sept. 14 to 16, 2000 we used the near infrared spectrometer and camera OSIRIS attached to the 4m Blanco telescope at Cerro Tololo Inter-American Observatory (CTIO), Chile, to observed BRI 0019-1522, BR 0103+0032, PSS J0248+1802, Q 2050–359, and BRI 2237-0607. The seeing was typically  $\sim 0''.8$  during these three nights. The detector was a  $1024 \times 1024$  Hawai'i HgCdTe array ( $18.5\mu\text{m}/\text{pixel}$ ). We used OSIRIS in the low-resolution cross-dispersed mode with a longslit of  $1''.2 \times 30''$ . The pixel scale was  $0''.403/\text{pixel}$ . In the cross-dispersed mode the J, H, K bands are recorded in adjacent orders in a single exposure yielding the entire near infrared wavelength range, i.e.,  $(\sim 0.9 - 2.5)\mu\text{m}$ . Making use of the long-slit mode we placed the object at seven different locations along the slit, separated by  $3''$  each for subsequent exposures to optimize the sky-correction. For flux calibration and correction of the strong atmospheric absorption bands, separating the J- and H-band and the H- and K-band, respectively, and additional weaker atmospheric (absorption) features we observed standard stars several times during each night (Elias et al. 1982; Perryman et al. 1998). In Table 1 the exposure times for the quasars are given.

For each of the different individual exposure times of the science frames, i.e., quasars (200 sec, 300 sec) and standard stars (3 sec to 20 sec), we recorded 20 to 25 dark frames. They were used to calculate average dark frames for each specific exposure time. The quasar and standard star spectra were dark corrected, subtracting the average dark frame of the corresponding exposure time.

Flatfield frames were taken in the lamp-on and lamp-off mode, both with 200 and 300 seconds integration time, respectively. The average lamp-off mode frames were subtracted from the aver-

age lamp-on mode frames to correct for the thermal background. These thermal background corrected mean flatfield frames were split up into separate 2D spectra for the J, H, and K band spectrum. Those were used to compute normalized flatfield frames (Horne 1986) which we employed for 2D flatfield correction for each individual spectral band.

For wavelength calibration we took helium-argon-neon comparison spectra. The location of the emission lines in the individual calibration frames differ by less than  $\lesssim 0.1$  pixel compared to each other. Therefore, an average calibration frame was computed and was used for the wavelength calibration. The uncertainty of the wavelength calibration is  $\Delta\lambda \sim 0.3\text{\AA}$ . The spectral overlap of the individual spectral bands is of the order of  $\sim 350\text{\AA}$  in the quasars restframe which allow a solid intercalibration to obtain a continuous spectrum of the near infrared wavelength range. The achieved spectral resolution amounts to  $R \simeq 1300$  in J, H, and K-band, respectively, based on the measured FWHM of strong night sky emission lines and isolated lines of the wavelength calibration frames.

We corrected each frame individually for the night sky intensity. For this purpose a  $3^{rd}$  order polynomial fit was calculated for each wavelength element to fit the spatial intensity distribution of the night sky emission. The fit was based on two regions,  $2''$  to  $20''$  wide, depending on the location of the object along the slit. These regions were separated by  $\sim 10''$ .

To derive a sensitivity function we assumed that the IR spectral energy distribution of a A-type and G-type star can be described with a black body spectrum of a specific  $T_{eff}$ . We used the black body temperatures given by Kurucz (1992) for the different spectral types of the stars we observed. We applied  $T_{eff} = 5850\text{K}$  (HD 1205, HD 25402, HD 198678),  $T_{eff} = 8250\text{K}$  (HD 19904, HD 205772), and  $T_{eff} = 8790\text{K}$  (HD 2811) to compute a black body spectrum for the observed wavelength range. The black body spectra were scaled to match the apparent magnitudes of the observed standard stars in the J-, H-, and K-band. For HD 2811, HD 19904, and HD 205772 we used the J, H, and K magnitudes given by Elias et al. (1982), while for HD 1205, HD 25402, and HD 198678 we had to calculate the apparent

near infrared magnitudes based on the apparent V-band magnitude. A sensitivity curve was calculated for each standard star. In general, the sensitivity functions given by the individual stars are nearly identical in shape and strength, within less than 2%. However, for a  $\sim 200\text{ \AA}$  wide region at the beginning and the end of each spectral wavelength range they differ less than  $\sim 20\%$ . But these regions fall into the strong absorption bands which separate the J, H, and K-band. We used the individual sensitivity functions obtained from the standard stars, we observed, to compute a mean sensitivity function for each wavelength range.

The quasar spectra were extracted using an optimal extraction algorithm (Horne 1986). The width of the spatial profile for the quasar spectra was the same as measured for the stars because high-redshift quasars can be treated as point sources. The individual spectra of the quasars were flux calibrated employing the mean sensitivity function of the corresponding spectral band. To correct for cosmic-ray events the individual 1D spectra were compared with each other. A weighted mean spectrum was calculated for each quasar. The weight was given by the mean signal-to-noise ratio in the continuum across the spectrum. The mean quasar spectra were corrected for atmospheric absorption using appropriately scaled transmission functions provided by observed spectra of the standard stars. The flux calibrated quasar spectra observed with OSIRIS at the 4m Blanco telescope are shown in Figure 1.

### 2.3. Paranal VLT/ISAAC Observation

The high-redshift quasar SDSS 1204–0021 ( $z = 5.03$ ; Fan et al. 2000) was observed in service mode with ISAAC attached to the VLT UT1 *Antu* in the H-band spectral range. The seeing was estimated from the spatial profile of standard star spectra to  $\sim 1''.1$  (April 11, 2001) and  $\sim 1''.2$  (June 14, 2001). A Hawai'i  $1024 \times 1024$  array from Rockwell was used in the longslit mode ( $1'' \times 120'', 0''.147/\text{pixel}$ ). We varied the location of the object along the slit by  $60''$  (with an additional random offset within  $5''$  for subsequent exposures to optimize the sky correction). For flux calibration and correction of the strong atmospheric absorption bands at the beginning and end of the H-band spectrum a standard star was observed each night. On April 10 and June 14, 2001, respectively, ten

quasar spectra with 180 sec exposure time were recorded which results in a total exposure time of 1 hr (Table 1).

For each night three dark frames with 5 sec (mean of 10 individual exposures) and 180 sec exposure time (mean of 3 individual exposures) were recorded. These frames were averaged for the corresponding exposure time and used for dark correction. Flatfield frames were taken in the lamp-on and lamp-off mode for each night. The lamp-off mode frames were subtracted from the adjacent lamp-on mode frame. The resulting flatfield frames were averaged and were normalized to apply a 2D flatfield correction.

Argon-xenon comparison spectra were recorded for wavelength calibration. The wavelength range amounts to  $\sim 14175$  to  $19040\text{ \AA}$  (April 10) and  $\sim 14195$  to  $19065\text{ \AA}$  (June 14) with a stepsize of  $\sim 4.8 \pm 0.5\text{ \AA}/\text{pixel}$ . The wavelength calibration is based on 20 individual lines. The spectral resolution, measured using the FWHM of strong night sky emission lines and isolated lines in the argon-xenon spectra, amounts to  $R \simeq 570$ .

We subtracted the night sky intensity for each spectrum individually. A 3<sup>rd</sup> order polynomial fit was calculated for each wavelength element to describe the spatial intensity distribution of the night sky emission. The fit based on two regions,  $\sim 25''$  and  $\sim 80''$  wide, which were separated by  $\sim 8''$ .

To derive a sensitivity function the standard stars HD 87097 (April 10) and HD 143567 (June 14) were observed. We used the black body temperatures given by Kurucz (1992) with  $T_{\text{eff}} = 5850\text{ K}$  (HD 87097, G3V) and  $T_{\text{eff}} = 10700\text{ K}$  (HD 143567, B9V) to compute a black body spectrum for the H-band range. These black body spectra were scaled to match the apparent magnitudes of the observed standard stars. A sensitivity curve was calculated for each standard star based on the V-band magnitude.

The spectra of the quasars which can be regarded as point sources, were extracted using an optimal extraction algorithm. The width of the spatial profile for the quasar spectra was the same as measured for the standard stars.

The individual spectra of SDSS 1204–0021 were flux calibrated employing the corresponding sensitivity function. To correct for cosmic-ray

events the individual 1D spectra were compared with each other. For each quasar a weighted mean spectrum was calculated. The weight was given by the mean signal-to-noise ratio in the continuum across the spectrum. The mean quasar spectra were corrected for atmospheric absorption using appropriately scaled transmission functions provided by observed spectra of the standard stars. Finally, the spectra obtained in April and June 2001 were averaged according to the signal-to-noise ratio in the continuum. In Figure 2 the flux calibrated H-band spectrum of SDSS 1204–0021 is shown.

#### 2.4. Composite Quasar Spectra

The analysis of composite spectra has the advantage of more clearly representing the average properties of the sample used to calculate each composite. We recently compiled a large sample of rest-frame ultraviolet and optical spectra for more than 800 type 1 AGNs (Dietrich et al. 2002b). About  $\sim 300$  of these spectra cover the ultraviolet Fe II – Mg II range ( $\lambda\lambda 2000 – 3000 \text{ \AA}$ ). A large fraction of the spectra were obtained by several groups for different studies over the last 20 years using ground-based instruments as well as *International Ultraviolet Explorer (IUE)* and *Hubble Space Telescope (HST)*. In addition, we retrieved all publicly available AGN spectra from the *HST* MAST archive. The type 1 AGNs (i.e., Seyfert 1 and quasars) of the sample cover a redshift range of  $0 \lesssim z \lesssim 5$  and nearly 6 orders of magnitude in luminosity. We excluded Broad-Absorption Line quasars (BAL QSOs) when calculating the composite spectra, although there are indications that BAL QSO emission line properties do not differ from non-BAL quasars (Weymann et al. 1991).

We analyzed these composite spectra which we calculated to investigate continuum vs. emission line relations (Dietrich et al. 2002b) for the Fe II/Mg II ratio. We selected a narrow luminosity range to calculate composite spectra for different redshift bins with nearly constant luminosity (the redshift sample). The location of this luminosity range was chosen to achieve a comparable number of individual quasars contributing to each redshift bin in the  $z - \lambda L_\lambda(1450 \text{ \AA})$  plane. We used a luminosity range of  $46.16 \leq \log \lambda L_\lambda(1450 \text{ \AA}) \leq 47.16 \text{ erg s}^{-1}$  (i.e.,  $43.0 \leq \log L_\lambda(1450 \text{ \AA}) \leq 44.0$ ). This range contains 323 quasars with  $z \geq 0.5$  and an av-

erage luminosity of  $\log \lambda L_\lambda(1450 \text{ \AA}) = 46.67 \pm 0.12 \text{ erg s}^{-1}$ . We computed composite spectra for redshift bins with  $\Delta z = 0.5$  centered on redshift  $z = 0.75, 1.25, \dots, 4.25$ , and  $4.75$ , respectively (Dietrich et al. 2002b). The composite spectra characterized by nearly constant luminosity provide valuable Fe II/Mg II measurements as a function of redshift. The quasar sample was also divided into 11 subsets with respect to the luminosity  $L_\lambda(1450 \text{ \AA})$  (the luminosity sample, see Table 2). Except for the lowest luminosity bin, each composite spectrum covers a range of  $\Delta \log \lambda L_\lambda = 0.5$  in luminosity starting at  $\log \lambda L_\lambda(1450 \text{ \AA}) = 43.16 \text{ erg s}^{-1}$ . The composite spectra with increasing luminosity yield information on the Fe II/Mg II ratio as a function of luminosity.

#### 3. Fitting of the Quasar Spectra

To measure the Fe II and Mg II emission strengths, we first transformed the individual high-redshift quasar spectra into the restframe. Although the Mg II  $\lambda 2798$  emission line doublet sometimes appears to be relatively isolated in quasar spectra, the superposition of many thousands of discrete ultraviolet Fe II emission lines forms broad emission blends (e.g., Wills et al. 1985, hereafter WNW85; Verner et al. 1999; Sigut & Pradhan 1998, 2003), which tend to blend with the broad base of Mg II complicating the measurement of Mg II and Fe II. Because of the line blending and the related difficulty defining the continuum level, these lines cannot be measured individually. However, as demonstrated by WNW85, it is possible to obtain the Fe II emission strength in a multi-component fit approach. Therefore, we assumed our observed quasar spectra ( $z=3.4$  and  $z=4.5$  sample), as well as the composite quasar spectra to consist of a superposition of the following four components, (i) a power law continuum ( $F_\nu \sim \nu^\alpha$ ), (ii) Balmer continuum emission, (iii) a pseudo-continuum due to merging Fe II emission blends, and (iv) an emission spectrum of other individual broad emission lines, such as Mg II. The power law continuum fit to the individual and composite quasar spectra was iteratively determined taking into account the measured strength of the Fe II emission and Balmer continuum emission derived by the fitting process. We already applied this multi-component fit approach successfully to a small sample of high redshift quasars

at  $z \simeq 3.4$  (Dietrich et al. 2002a).

### 3.1. Non-stellar Continuum

We first determined the underlying non-stellar power law continuum, component (i), from spectral windows which are free (or almost free) of contributions by the components (ii) to (iv). For this purpose it is very important that the spectrum covers a wide wavelength range. The high-redshift quasars we observed allow us to use a 20 Å wide continuum window, centered at  $\lambda_c \simeq 4000 \pm 50$  Å which is nearly free of emission line contamination and hydrogen Balmer continua. Only minor Fe II emission can be expected for this wavelength region (WNW85; Verner et al. 1999; Corbin & Boroson 1996) and hence will not significantly affect the continuum setting. For 4 of the individual high-redshift quasars (BRI 0019-1522, BR 0103+0032, PC 1158+4635, BRI 2237-0607) we have also rest-frame UV spectra. These spectra provide continuum windows at  $\lambda\lambda \simeq 1330 - 1380$  Å, and  $\lambda\lambda \simeq 1440 - 1470$  Å, and  $\lambda\lambda \simeq 1685 - 1695$  Å which are nearly uncontaminated by line emission as well (Francis et al. 1991). For those quasars for which we had no access to the short wavelength UV part of the spectrum (PSS J0248+1802, Q 2050-358) we used continuum windows at  $\sim 2230$  Å to estimate the continuum strength. The UV data allow us even better constraints on the non-stellar continuum strength for these objects. The uncertainty introduced by estimating the continuum level, based on at least two of the spectral ranges described above, is estimated to be of the order of less than  $\sim 10\%$ .

### 3.2. Balmer Continuum

To estimate the Balmer continuum emission spectrum for our fits we assumed gas clouds of uniform temperature ( $T_e = 15000$  K) which are partially optically thick. In this case the Balmer continuum spectrum ( $\lambda \lesssim 3646$  Å) can be described by

$$F_\lambda^{BaC} = F^{BE} B_\lambda(T_e) (1 - e^{-\tau_\lambda}); \quad \lambda \leq \lambda_{BE}$$

with  $B_\lambda(T_e)$  as the Planck function at the electron temperature  $T_e$ ,  $\tau_\lambda$  as optical depth at  $\lambda$ , and  $F^{BE}$  as a normalized estimate for the Balmer continuum flux density at the Balmer edge at

$\lambda = 3646$  Å (Grandi 1982). The strength of the Balmer continuum emission can be estimated from the flux density at  $\lambda \simeq 3675$  Å, after subtraction of the power-law continuum component, since at this wavelength there is no significant contamination by Fe II emission (WNW85; Verner et al. 1999). The  $\lambda 3675$  Å restframe flux density level was therefore used to normalize the Balmer continuum spectrum. At wavelengths  $\lambda \geq 3646$  Å higher order Balmer lines are merging to a pseudo-continuum, yielding a smooth rise to the Balmer edge (WNW85). We used the results of the model calculations provided by Storey & Hummer (1995) (case B,  $T_e = 15000$  K,  $n_e = 10^8 - 10^{10}$  cm $^{-3}$ ) to estimate the strength of high order Balmer emission lines, assuming a Gaussian profile for each high order Balmer line (FWHM = 3000 km s $^{-1}$ ). We calculated several Balmer continuum spectra for  $T_e = 15000$  K and  $0.1 \leq \tau_\lambda \leq 2$  to obtain Balmer continuum emission templates. These Balmer continuum templates were supplemented for  $\lambda > 3646$  Å with high order Balmer emission lines with  $10 \leq n \leq 50$ , i.e., H $\vartheta$  and higher.

### 3.3. Fe II Emission

Calculating the Fe II emission spectrum is much more difficult and the influence of unknown parameters such as internal turbulence velocities, emission line transport, pumping by the incident continua, line fluorescence, and metallicity, which affect the emergent Fe II spectrum, are still not well understood (e.g., WNW85; Netzer et al. 1985; Joly 1987; Bautista & Pradhan 1998; Sigut & Pradhan 1998; Verner et al. 1999; Collin & Joly 2000). In spite of these uncertainties it has been shown that the Fe II emission strength of Seyfert 1 galaxies and quasars can be measured using empirically derived Fe II emission template spectra (WNW85; Laor et al. 1997; McIntosh et al. 1999; Dietrich et al. 2002a; Iwamuro et al. 2002). We fitted the Fe II emission in our quasar spectra using scaled and broadened empirical Fe II emission template spectra to derive relative Fe II emission strength values. For the ultraviolet wavelength range these templates had been carefully extracted from *HST* observations of I Zw1 by Vestergaard & Wilkes (2001). These emission templates include contributions of Fe II and Fe III. In the fitting process the strength and the broadening of the Fe emission template are free parameters.

The use of different empirical Fe II emission templates, in particular in the range of the broad Mg II $\lambda 2798$  emission line, introduces additional uncertainty to measured Fe II/Mg II ratios. For example, the empirical Fe emission template we use in our analysis underestimates the Fe flux in the region. Vestergaard & Wilkes (2001) set the flux level beneath the broad Mg II $\lambda 2798$  emission line to zero in the Fe template extracted from IZw 1. This approach is reasonable since detailed model calculations (Verner et al. 1999; Sigut & Pradhan 2003) indicate that the Fe flux level in this wavelength range is of the order of only 15 to 20 % compared to neighboring Fe emission. The treatment of the Fe emission beneath Mg II line has a major impact on the Mg II flux. Since the broad component can contain  $\sim 50$ –80 % of the total line flux, by neglecting the presence of the broad profile component can easily cause an underestimate of the Mg II flux by a factor of  $\sim 2$  (Vestergaard & Wilkes 2001; Dietrich et al. 2002b).

We explored the effects of non-zero Fe II fluxes beneath the Mg II emission line. The gap in the Fe emission template, we used for the analysis (Vestergaard & Wilkes 2001), was replaced by a low order polynomial (2<sup>nd</sup> order) which minimal flux level accounts to  $\sim 15$  % of the immediately close by located Fe emission peaks. This choice is motivated by the photoionization calculations mentioned above (Verner et al. 1999; Sigut & Pradhan 2003). This additional flux increases the integrated Fe II flux in the range  $\lambda\lambda 2200$ –3090 Å by less than 2 %. Hence, the integrated Fe II flux is nearly unchanged by filling the gap beneath the Mg II line with a more realistic estimate of the complex Fe II emission.

To estimate the implications of the modified Fe emission template on the measured Mg II $\lambda 2798$  emission line strength we re-analyzed the Mg II line profile in each individual high-redshift and composite quasar spectra. The line profile was fit with a narrow and a broad Gaussian component. The narrow component was nearly unchanged. The strength of the broad component was reduced by  $\sim 6$  % on average. The cumulative effect of the slightly increased Fe II emission and the reduced strength of the Mg II emission flux amounts to  $\sim 10$  % increase for the measured Fe II/Mg II ratios, nearly independent of the Mg II profile width.

### 3.4. Strong Broad Emission Lines

The broad emission line profile of Mg II $\lambda 2798$  was fit after subtracting the power law continuum, the Fe II emission, and the Balmer continuum emission. Generally, the Mg II $\lambda 2798$  emission line profile could be reconstructed with two Gaussian components, a narrow component (FWHM(Mg II) =  $2270 \pm 570$  km s $^{-1}$ ) and a blueshifted broad component ( $\Delta v \simeq -1000$  km s $^{-1}$ , FWHM(Mg II) =  $6300 \pm 1300$  km s $^{-1}$ ). The approach to reconstruct the Mg II emission line profile with two Gaussian components was only chosen to measure the line flux; each individual component has no physical meaning by itself.

### 3.5. Internal Reddening

In recent years growing evidence has appeared for the presence of large amounts of dust ( $M_{dust} \gtrsim 10^8 M_{\odot}$ ) in the host galaxies of high-redshift quasars (e.g., Guilloteau et al. 1997, 1999; Carilli et al. 2000; Omont et al. 2001). It is assumed that the dust is distributed in a kiloparsec-scale warped disk (Sanders et al. 1989) which is illuminated by the central AGN. The observed dust emission spectra from 3 to 30  $\mu$ m can be explained by such a model as shown by Andreani et al. (1999) and Willott et al. (2000). However, since the presented spectra are typical quasar spectra with prominent broad emission lines, it is unlikely that the broad-line region (BLR) is significantly blocked by dust (e.g., Netzer & Laor 1993). Even if the radiation has to pass through an (external) dust screen the extinction of the Mg II and the UV Fe II-emission (having about the same mean wavelength) will be comparable and the line ratio is not expected to be significantly modified.

### 3.6. Multi-Component Fit of the Quasar Spectra

We have analyzed the individual high-redshift quasar spectra, as well as the composite quasar spectra in a multi-component fit approach using emission templates as described above. The spectra are transformed to their restframe using the corresponding redshift given in Table 2. The quasar spectra were iteratively fitted first with a power law continuum, then a Balmer continuum emission template and an Fe emission template were employed, and finally a two Gaussian pro-

file fit was used to measure the broad  $\text{Mg II}\lambda 2798$  emission line. The strength of the Fe emission templates was varied, as well as the width of the individual iron features. The broadening of the empirical Fe emission template (Vestergaard & Wilkes 2001), was achieved by convolution with a Gaussian profile. The width of the iron emission features of the best fit is consistent with the profile width of the  $\text{C IV}\lambda 1549$  and  $\text{Mg II}\lambda 2798$  emission lines to within  $\sim 1000 \text{ km s}^{-1}$ . We also varied the strength and the optical depth  $\tau_\lambda$  of the Balmer continuum emission ( $0.1 \leq \tau_\lambda \leq 1.0$ ). Minimal  $\chi^2$  fits were calculated to determine the best fit. In order to estimate the accuracy of our fits, we also calculated fits for settings of different parameters around the best fit values. From the widths of the resulting  $\chi^2$  distributions we estimated mean errors for these parameters which were employed to estimate the uncertainties of the flux measurements. In spite of a signal-to-noise ratio of  $S/N \simeq 10$  in the continuum of the individual high-redshift quasar spectra, the UV Fe II and Mg II emission strength can be measured to within  $\sim 12 - 20\%$  (Fe II) and  $\sim 10\%$  (Mg II), respectively. The errors of the Fe II/Mg II ratio determined for the composite spectra also take into account the uncertainties introduced by the individual spectra that contribute to the corresponding composite spectrum. We estimated this uncertainty from the rms-spectrum which is computed for each composite spectrum.

#### 4. Results

In Figure 1 we present the quasar spectra of the  $z = 4.5$  sample together with the power law continuum fit, the appropriately scaled Fe and Balmer continuum emission templates, and the fit of the  $\text{Mg II}\lambda 2798$  emission line. The achieved multi-component fit results benefit significantly from the large covered wavelength range to define a reliable continuum fit, in contrast to prior studies. The residuum, subtracting the best fit from the quasar spectrum, is displayed in the bottom panel for each quasar. The remaining quite strong feature in the residuum spectra at  $\lambda \simeq 3200 \text{ \AA}$  is due to prominent iron emission blends, multiplets M6 and M7, that is not covered by the Fe template which we are using. The ultraviolet Fe II emission line flux was measured from the scaled Fe templates for a wavelength range of  $\lambda\lambda 2200 - 3090 \text{ \AA}$ .

The integrated flux of  $\text{Mg II}\lambda 2798$  was determined from the two component Gaussian fit. The measured flux for both emission features are given in Table 2.

For SDSS 1204–0021 only the H-band spectral range was observed. Instead of applying an uncertain multi-component fit – the continuum strength and the contribution of the Balmer continuum emission can not be reliably determined – we compared the strength of the  $\text{Mg II}\lambda 2798$  and the broad Fe II emission feature at  $\lambda \simeq 2500 \text{ \AA}$  with the quasars at  $z \simeq 4.5$ . We calculated a mean  $z \simeq 4.5$  quasar spectrum based on the other quasars of the  $z = 4.5$  sample. In Figure 2 the spectrum of SDSS 1204–0021 transformed to the restframe is shown together with the mean  $z \simeq 4.5$  quasar spectrum. This mean high-redshift quasar spectrum was scaled by multiplying with a constant to match the spectrum of SDSS 1204–0021. The difference spectrum is displayed in the bottom panel of Figure 2. The overall spectral slopes of both these spectra are very similar. Since the spectra were scaled to match the overall spectral shape a small residuum is left of Mg II emission. The Mg II emission line profile is significantly broader in SDSS 1204–0021 ( $FWHM \simeq 7400 \text{ km s}^{-1}$ ) than in the mean  $z \simeq 4.5$  quasar spectrum ( $FWHM \simeq 3000 \text{ km s}^{-1}$ ) and it does not show a pronounced narrow component. Although the profiles of Mg II look quite different this is predominantly due to the missing narrow component in SDSS 1204–0021, as can be seen in the difference spectrum (Fig. 2, bottom panel). The residual flux in the difference spectrum amounts to  $\sim 5\%$  of the total Mg II flux in both quasar spectra. Although the Fe II/Mg II ratio can not be measured in a multi-component fit, the comparison with the mean  $z \simeq 4.5$  quasar spectrum indicates that the ratio should be very similar to the mean value of the individual quasars at  $z > 4$ .

##### 4.1. Fe II/Mg II Ratio as a Function of Redshift

First, we compare the Fe II/Mg II ratios for the  $z = 3.4$  and  $z = 4.5$  quasar sample we observed for individual quasars. The measured Fe II/Mg II ratios which are given in Table 2, are displayed as function of redshift in Figure 3. The results for the quasars of the  $z = 3.4$  sample (Dietrich et al. 2002a) are supplemented with Q 2050–359

( $z = 3.51$ ) which we observed at CTIO. There is obviously no strong indication for an evolution of the Fe II/Mg II ratio from  $z \simeq 3.2$  up to  $z \simeq 4.8$ . Including the result of the comparison of the SDSS 1204–0021 spectrum with the mean  $z = 4.5$  quasar spectrum, the Fe II/Mg II ratio shows no variation up to  $z \simeq 5$ . Although our observation of PC 1158+4635 indicates a lower Fe II/Mg II ratio, SDSS 1204–0021 and recent NICMOS/HST observations of three  $z \simeq 6$  quasars show no declining Fe II/Mg II ratio (Freudling et al. 2003).

To investigate the evolution of the Fe II/Mg II ratio over a wide range in cosmic time, particularly from the local universe to  $z \simeq 5$ , we measured this emission line ratio in the quasar spectra of the redshift sample. The criterion of nearly constant and also comparable luminosity of the composite spectra of this sample (Table 2) compared to the  $z = 3.4$  and  $z = 4.5$  quasar samples minimizes luminosity effects on the emission line strength like the Baldwin effect (e.g., Osmer & Shields 1999; Croom et al. 2002; Dietrich et al. 2002b; Shang et al. 2003). The Mg II $\lambda 2798$  and UV Fe II line fluxes we measure for the quasars of the redshift sample are given in Table 2. In Figure 3 these Fe II/Mg II ratios are plotted together with the results for the individual high-redshift quasars. The analysis of the redshift quasar spectra provides further evidence that the ratio of iron to  $\alpha$ -elements expressed by Fe II/Mg II lacks an evolution for luminous quasars from the local universe ( $z \simeq 0$ ) up to  $z \simeq 5$ , i.e., an cosmic age of  $\sim 1$  Gyr (Fig. 3).

#### 4.2. Fe II/Mg II Ratio as a Function of Luminosity

To investigate the dependence of the Fe II/Mg II ratio on luminosity we analyzed the composite quasar spectra of the luminosity sample which cover nearly  $\sim 6$  orders of magnitude in luminosity (Dietrich et al. 2002b). In Figure 4 the Fe II/Mg II ratios measured for these composite spectra (luminosity sample) are displayed as a function of continuum luminosity  $\lambda L_\lambda(1450)$ . In addition, the Fe II/Mg II ratios of the individual high-redshift quasars of the  $z = 3.4$  and  $z = 4.5$  samples are shown. Within the errors there is a weak trend for a higher Fe II/Mg II ratio towards higher luminosities (Fig. 4). It appears that the ratio is nearly constant for  $\log \lambda L_\lambda(1450 \text{ \AA}) \lesssim 45$   $\text{erg s}^{-1}$  with Fe II/Mg II =  $2.1 \pm 0.3$  and amounts to

Fe II/Mg II =  $4.0 \pm 0.8$  at higher luminosities. The composite quasar spectrum at  $\log \lambda L_\lambda = 43.51$   $\text{erg s}^{-1}$  consists of only 3 individual spectra from which two cover the UV Fe II – Mg II wavelength range. One of these two quasars is WPVS007, a well-known narrow-line Seyfert 1 (NLS1) galaxy. The *HST* spectrum that we retrieved from the *HST* data archive, shows exceptionally strong Fe II emission (Grupe et al. 1995) which is a common characteristic of NLS1 galaxies (e.g., Mathur 2000; Pogge 2000). Thus WPVS007 dominates the composite spectrum at  $\log \lambda L_\lambda = 43.51 \text{ erg s}^{-1}$  and results to the high value of Fe II/Mg II =  $5.6 \pm 1.2$ .

#### 4.3. Comparison with other Studies

During the last few years there have been a few similar studies of the UV Fe II/Mg II ratio in quasars at high redshifts (e.g., Kawara et al. 1996; Taniguchi et al. 1997; Murayama et al. 1999; Thompson et al. 1999; Iwamuro et al. 2002; Freudling et al. 2003), as well as for lower redshift samples (Wills et al. 1980; Grandi 1981; Wills et al. 1985). However, to compare those results with the Fe II/Mg II ratios we measure here ( $z = 3.4$ ,  $z = 4.5$ , and redshift and luminosity quasar samples), it is necessary to adjust the published ratios to reflect the same spectral range we used to measure the Fe II emission (see below). The comparison is further complicated by the different Fe II emission templates which were used to measure the Fe II flux, as well as taking into account the contribution of the Balmer continuum. Wills et al. (1985) applied an Fe II emission template based on their photoionization model calculations (Netzer & Wills 1983), while Thompson et al. (1999) and Iwamuro et al. (2002) used the LBQS mean quasar spectrum (Francis et al. 1991) to extract an empirical Fe II emission template. Another more serious uncertainty is introduced by the generally restricted wavelength coverage of prior studies that made a proper definition of the underlying continuum strength very difficult, in particular, in the restframe UV wavelength range of high-redshift quasars. The quasar spectra Wills et al. (1985) analyzed covered at least the spectral range from C III] $\lambda 1909$  up to H $\beta$   $\lambda 4861$ . The high redshift quasars ( $z = 3.4$  and  $4.5$  samples) in the Thompson et al. (1999) study cover  $\sim 600 \text{ \AA}$  around the Mg II $\lambda 2798$  emission line and, hence, does not cover the entire Fe II bump. The in-

dividual spectra of the Thompson et al. sample have been re-analyzed by Iwamuro et al. (2002), who also observed the Mg II – UV Fe II wavelength range for 13 quasars with  $z \gtrsim 4.4$ , across a wavelength range of  $\sim 1200 \text{ \AA}$ . Iwamuro et al. (2002) also presented measurements of Fe II/Mg II for the early data release of the SDSS QSO survey, as well as for quasar spectra retrieved from the *HST* and *IUE* data archives for a local quasar population. Recently, Freudling et al. (2003) presented results of measured Fe II/Mg II ratios for three quasars at  $z \simeq 6$ . Although the uncertainties are quite large the Fe II/Mg II ratios are comparable to the results of the  $z \gtrsim 4$  quasars both here and by Iwamuro et al. (2002).

To reduce the most obvious source of differences for the individual published Fe II/Mg II ratios we adjusted the Fe II/Mg II emission line ratios of prior studies to the integration window that we used to measure the Fe II emission line flux. Therefore, we compared the Fe emission flux we measured for the integration range we used ( $\lambda\lambda 2200 - 3090 \text{ \AA}$ ) with the those resulting by applying different integration windows. (WNW85; Thompson et al. 1999; Iwamuro et al. 2002).

In Figure 5 we present our measurements of the Fe II/Mg II ratio for the  $z = 3.4$ ,  $z = 4.5$ , and redshift samples in comparison with the rescaled results presented by Wills et al. (1985), Thompson et al. (1999), Iwamuro et al. (2002), and Freudling et al. (2003). At higher redshifts ( $z \gtrsim 3$ ) the intercalibrated Fe II/Mg II ratios are quite consistent although the scatter of the individual measurements given by Iwamuro et al. (2002) is large. In particular, the Fe II/Mg II ratios for the high-redshift ( $z \gtrsim 4$ ) composite spectra of the SDSS sample which are also those with the highest luminosity of this sample (Iwamuro et al. 2002) agree quite well with the results of our composite spectra (Fe II/Mg II  $\simeq 4.4$  to 5.7 compared to  $5.4 \pm 1.3$  here, Table 2). The Fe II/Mg II measurements for three quasars at the highest redshift indicate that comparable high Fe II/Mg II ratios can be found up to redshifts of  $z \simeq 6$  (Freudling et al. 2003). However, the scatter of the Fe II/Mg II ratios at  $z \gtrsim 4$  given in these studies is quite large. We presume that a significant fraction of the large range of these measured Fe II/Mg II ratios is caused by the restricted wavelength coverage of the analyzed quasar spectra. Although the mathematically best solution

was determined for the multi-component fit, the continuum strength appears in some cases not well defined, yielding quite uncertain Fe II flux measurements. Some scatter in the Fe II/Mg II ratio given in recent studies may also be introduced by using emission lines that are not completely covered by the available spectra or measured at all, instead has been estimated from the C III] $\lambda 1909$  emission blend (Freudling et al. 2003).

In general, at lower redshifts ( $z \lesssim 2$ ) the Fe II/Mg II ratios derived from the SDSS quasar spectra ( $2.6 \pm 0.3$ ) are in good agreement with the ratios we measured ( $2.1 \pm 0.3$ ) from the composite spectra of  $z \lesssim 1$  quasars with lower luminosities (see Fig. 4, luminosity sample,  $\log \lambda L_\lambda(1450 \text{ \AA}) \lesssim 45 \text{ ergs}^{-1}$ ). The sample of quasars studied by Wills et al. (1985) with  $z \lesssim 0.8$  infer Fe II/Mg II ratios which also are quite consistent with the ratios we derived. However, the intercalibrated Fe II/Mg II ratios based on the SDSS quasars are significantly lower than the ratios we determined from composite spectra of nearly constant luminosity for redshifts less than  $z \simeq 2$  (Fig. 5). A possible explanation may be given by the lower luminosity of these SDSS quasars compared to our composite quasar spectra in this redshift range with  $\log \lambda L_\lambda(1450 \text{ \AA}) \simeq 46.7 \text{ ergs}^{-1}$  for the following reasons. Although the Mg II $\lambda 2798$  and Fe II emission may both originate in the partially ionized zone of the line emitting region, both lines depend in different ways on the conditions of this region, e.g., radiative transfer, destruction by Balmer continuum absorption, and conversion to optical Fe II emission (e.g., Wills et al. 1985; Joly 1987; Verner et al. 1999). Luminosity dependent variations in the SED of the AGN continuum, in particular of the ionizing continuum, are known to exist based on observational and theoretical studies (e.g., Netzer et al. 1992; Laor et al. 1995; Wandel 1999; Dietrich et al. 2002b). Hence, quasars of different luminosity may have a different continuum SED which may result in slightly different conditions of the Fe II and Mg II $\lambda 2798$  emitting region ( $z \lesssim 2$ ). Taking the sensitive dependence of Fe II and Mg II $\lambda 2798$  on the conditions of the gas into account this may result in a wide range of possible Fe II/Mg II ratios as observed at low redshifts ( $z \lesssim 0.2$ ). The large scatter of the Fe II/Mg II ratio also may emphasize that it is important to compare this line ratio for quasars of similar luminos-

ity.

## 5. Discussion

The Fe II/Mg II emission line ratios which we find for our high-redshift quasar sample, as well as for the composite quasar spectra are consistent with results presented by Wills et al. (1985), Thompson et al. (1999), Murayama et al. (1999), Dietrich et al. (2002a), Iwamuro et al. (2002), and Freudling et al. (2003). In particular, the Fe II/Mg II ratio at high redshifts shows similar strength compared to those measured in low redshift quasars ( $z \simeq 0.2$ ) of comparable luminosity (WN85). Assuming that the physical conditions in the BELR of quasars and that the spectral energy distribution of the ionizing continuum are independent of redshift the observed lack of evolution of the Fe II/Mg II emission ratio suggests that the observed relative abundance of iron, i.e. Fe/Mg, in the local universe is already achieved at redshifts  $z \gtrsim 4$ . This result indicates that an episode of intense star formation began before the observed quasar activity. Hence, the nearly constant Fe II/Mg II ratio over cosmic time has important implications on the star formation history, particularly at high redshifts since the age of the universe is less than  $\sim 1.3$  Gyr (for redshifts  $z \gtrsim 4.5$ ).

With this result, we can estimate the beginning of the first star formation in luminous quasar host galaxies, i.e., probably young massive elliptical galaxies from the evolution time scale of type Ia SNe and the resulting delay in the Fe enrichment. Evolutionary models of the Fe enrichment in a galaxy following the initial starburst has been calculated e.g. by Yoshii et al. (1998). Although, as pointed out by Yoshii et al., evidence that the initial mass function may have been different for the first stars makes such model calculations quantitatively somewhat uncertain, it is clear from these computations that the relative Fe abundance is rather low initially and starts to grow steeply about  $\sim 1$  Gyr after the beginning of the star formation, reaching a maximum (at about 3 Gyrs in the Yoshii et al. model), before declining to the local value (see also Matteucci & Padovani 1993; Hamann & Ferland 1993). The same temporal evolution of the Fe/Mg ratio is found for the giant elliptical galaxy model (M4a) presented by

Hamann & Ferland (1993). Their model predicts a strong increase of Fe/H at  $\sim 1$  Gyr after the beginning of the star formation, with the most rapid rise of the Mg/Fe ratio during the 1 - 1.38 Gyr period.

However, Matteucci (1994), Friaça & Terlevich (1998), and Matteucci & Recchi (2001) pointed out that the common assumption  $\tau_{\text{delay}} \simeq 1$  Gyr as a typical time scale for the enrichment delay of Fe, released by SNe type Ia SNe explosions, is only a rough estimate which based on the conditions of the solar neighborhood. The evolutionary models presented by Friaça & Terlevich (1998) and Matteucci & Recchi (2001) suggest that this delay depends crucially on environmental conditions of the star formation process and that it can be significantly shorter. They showed that for elliptical galaxies an intense early star formation episode with enhanced star formation rate and short star formation times scale results in a high SNIa rate which reaches a maximum already  $\sim 0.3 - 0.8$  Gyr after the beginning of the star formation, in contrast to  $\sim 4$  to 5 Gyr as for the solar neighborhood. Various theoretical studies have explored possible scenarios that SNe type Ia can, under certain conditions, also be produced by massive stars with a much shorter evolutionary time scale than that assumed in the standard scenarios (e.g., Yoshii et al. 1998), some SNe type Ia progenitors could have much shorter life times (e.g., Iben & Tutukov 1984; Smecker-Hane & Wyse 1992).

There is growing evidence that luminous quasars are residing in massive host galaxies (e.g., Kukula et al. 2001; Nolan et al. 2001; Dunlop et al. 2003), which at high redshift ( $z \gtrsim 3$ ) are probably young ellipticals or massive spheroidal systems in the process of forming (e.g., van Breugel et al. 1998; Papadopoulos et al. 2000; De Breuck et al. 2002). This would support the assumption of significantly shorter evolutionary time scales for the major iron enrichment in massive spheroidal galaxies than that generally cited,  $\tau_{\text{evol}} \simeq 1$  Gyr. As noted above, the significant release of iron by type Ia SNe to the interstellar medium can be as short as  $\tau_{\text{evol}} \lesssim 0.3 - 0.8$  Gyr. In addition, a more rapid evolution of progenitor stars to produce and release iron to the interstellar environment than previously assumed may be also possible. Recent models of galaxy formation, particularly in the early universe suggest that a rapid assem-

bly of (at least some) massive spheroidal systems was accompanied by intense star formation, and subsequent quasars activity (e.g., Kauffmann & Haehnelt 2000; Green et al. 2001; Romano et al. 2002). The indication of an early star formation epoch beginning at  $z_f \simeq 6 - 9$  is also consistent with cosmic structure formation models (Gnedin & Ostriker 1997) and with recent estimates of the epoch of reionization.

The observed lack of an evolving Fe II/Mg II ratio indicates that the star formation responsible for the chemical enrichment of the gas close to the quasar has started at least  $\tau_{evol}$  earlier. Therefore, the first major star formation epoch in high-redshift quasars ( $z \gtrsim 4.5$ ) started at  $z_f \simeq 6 - 9$ . It is interesting to note that this estimate is comparable to the epoch of re-ionization of the universe (?Haiman & Loeb 1998; Becker et al. 2001; Fan et al. 2002). The indication of an early intense star formation epoch is further supported by recent results of the Wilkinson Microwave Anisotropy Probe (WMAP) (Bennett et al. 2003). Cen (2003) suggests that the first stars were formed as early as  $z \gtrsim 15$  and that they re-ionize the universe for the first time, while a second re-ionization episode of the universe occurred at  $z \simeq 6$ .

## 6. Conclusion

We have observed 6 luminous high-redshift quasars ( $\gtrsim 4.4$ ) in the near infrared wavelength range to measure the Fe II/Mg II emission line ratio and thereby estimate the beginning of the first intense star formation. To explore the evolution of the Fe II/Mg II ratio over a wide redshift range, i.e. cosmic time, we measured this ratio for composite quasar spectra which cover a redshift range of  $0 \lesssim z \lesssim 5$  with nearly constant continuum luminosity (redshift sample), as well as for composite quasar spectra which span nearly  $\sim 6$  orders of magnitude in luminosity (luminosity sample). We find that the Fe II/Mg II ratio shows no evolution for cosmic times corresponding  $3.2 \lesssim z \lesssim 5.0$  compared to measurements for quasars at  $z = \simeq 3.4$  (see e.g., Dietrich et al. 2002a). The Fe II/Mg II ratio also shows no evolution from the local universe to very high redshifts ( $z \simeq 5$ ), corresponding to an age of the universe of  $\sim 1$  Gyr. For increasing continuum luminosities, however, we detect a weak trend for higher Fe II/Mg II ratio at higher

luminosities. It appears that at lower luminosities ( $\log \lambda L_\lambda(1450) \lesssim 10^{45} \text{ erg s}^{-1}$ )  $\text{Fe II/Mg II} \simeq 2$  while at higher luminosities ( $\log \lambda L_\lambda(1450) \gtrsim 10^{46} \text{ erg s}^{-1}$ )  $\text{Fe II/Mg II} \simeq 4 - 5$ .

Assuming that luminous quasars reside in massive galaxies, probably elliptical galaxies or in forming massive spheroidal systems in the early universe (e.g., Kauffmann & Haehnelt 2000; Kukula et al. 2001; Nolan et al. 2001; Romano et al. 2002; Dunlop et al. 2003) the lack of evolution in the observed Fe II/Mg II ratios across the redshift range  $0 \lesssim z \lesssim 5$  suggests that there is also no evolution in Fe/Mg in the quasar nuclear region. The actual value of Fe/Mg in quasar BELRs remains uncertain. Further modeling of the Fe II and Mg II line emission is required. However, there is some evidence that Fe/Mg is above solar in quasars at low to moderate redshifts (Wills et al. 1985). If that result is confirmed, the lack of evolution in Fe II/Mg II out to  $z \simeq 5$  reported here would indicate that the first major star formation in the environment of high-redshift quasars started at  $z_f \simeq 6 - 9$ , corresponding to an age of the universe of  $\sim 0.5$  Gyr. It is interesting to note that this epoch is comparable to the proposed time of the re-ionization of the universe (Haiman & Loeb 1998; Cen 2003).

This work was supported by NASA through their Long Term Space Astrophysics program (NAG5-3234), NSF AST99-84040, and an archival research grant from the Space Telescope Science Institute (AR-07988.01-96A). MV acknowledges financial support from the Columbus Fellowship and support for Proposal number AR-09549, provided by NASA through a grant from the Space Telescope Science Institute, which is operated by the Association of Universities for Research in Astronomy, Incorporated, under NASA contract NAS5-26555.)

## REFERENCES

Andreani, P., Franceschini, A., & Granato, G. 1999, MNRAS, 306, 161

Arnaud, K.A., Gilmore, G., & Cameron, A.C. 1989, MNRAS, 237, 495

Bautista, M.A. & Pradhan, A.K. 1998, ApJ, 492, 650

Becker, R.H., et al. 2001, AJ, 122, 2850

Bennett, C.L., et al. 2003, ApJ, 583, 1

Carilli, C.L., Bertoldi, F., Menten, K.M., et al. 2000, ApJ, 533, L13

Carilli, C.L., Kohno, K., Kawabe, R., et al. 2002, AJ, 123, 1838

Carroll, S.M., Press, W.H., & Turner, E.L. 1992, ARA&A, 30, 499

Cen, R. 2003, ApJ, in press, (astro-ph/0303236)

Cen, R. & Ostriker, J.P. 1999, ApJ, 519, L109

Collin, S. & Joly, M. 2000, New Astron.Rev., 44, 531

Connolly, A.J., Szalay, A.S., Dickinson, M., Subbarao, M., & Brunner, R.J. 1997, ApJ, 486, L11

Corbin, M.R. & Boroson, T.A. 1996, ApJS, 107, 69

Croom, S.M., et al. 2002, MNRAS, 337, 275

De Breuck, C., van Breugel, W., Stanford, S.A., Röttgering, H., Miley, G., & Stern, D. 2002, AJ, 123, 637

Dietrich, M., Appenzeller, I., Wagner, S.J., et al. 1999, A&A, 352, L1

Dietrich, M. & Wilhelm-Erkens, U. 2000, A&A, 354, 17

Dietrich, M., Appenzeller, I., Vestergaard, M. & Wagner, S.J. 2002a, ApJ, 564, 581

Dietrich, M., et al. 2002b, ApJ, 581, 912

Dietrich, M., et al. 2003a, A&A, 398, 891

Dietrich, M., et al. 2003b, ApJ, 589, 722

Dunlop, J.S., McLure, R.J., Kukula, M.J., Baum, S.A., O'Dea, C.P., & Hughes, D.H. 2003, MNRAS, 340, 1095

Elias, J.H., Frogel, J.A., Matthews, K., & Neugebauer, G. 1982, AJ, 87, 1029

Elston, R., Thompson, K.L., & Hill, G.J. 1994, Nature, 367, 250

Fan, X., et al. 2000, AJ, 119, 1

Fan, X., Narayanan, V.K., Strauss, M.A., White, R.L., Becker, R.H., Pentericci, L., & Rix, H.-W. 2002, AJ, 123, 1247

Ferland, G.J., Baldwin, J.A., Korista, K.T., et al. 1996, ApJ, 461, 683

Ferrarese, L. & Merritt, D. 2001, ApJ, 555, L79

Francis, P.J., Hewett, P.C., Foltz, C.B., et al. 1991, ApJ, 373, 465

Freedman, W.L., Madore, B.F., Gibson, B.K., et al. 2001, ApJ, 553, 47

Freudling, W., Corbin, M.R., & Korista, K.T. 2003, ApJ, 587, L67

Friaça, A.C.S. & Terlevich, R.J. 1998, MNRAS, 298, 399

Gebhardt, K., et al. 2000, ApJ, 543, L5

Gnedin, N.Y. & Ostriker, J.P. 1997, ApJ, 486, 581

Granato, G.L., Silva, L., Monaco, P., Panuzzo, P., Salucci, P., De Zotti, G., & Danese, L. 2001, MNRAS, 324, 757

Grandi, S.A. 1981, ApJ, 251, 451

Grandi, S.A. 1982, ApJ, 255, 25

Green, P.J., Forster, K., & Kuraszkiewicz, J. 2001, ApJ, 556, 727

Grupe, D., Beuermann, K., Mannheim, K., Thomas, H.-C., Fink, H.H., & de Martino, D. 1995, A&A, 300, L21

Guilloteau, S., Omont, A., McMahon, R.G., Cox, P., & Petitjean, P. 1997, A&A, 328, L1

Guilloteau, S., Omont, A., McMahon, R.G., Cox, P., & Petitjean, P. 1999, A&A, 349, 363

Haiman, Z. & Loeb, A. 1998, ApJ, 503, 505

Hamann, F. 1997, ApJS, 109, 279

Hamann, F. & Ferland, G.J. 1992, ApJ, 381, L53

Hamann, F. & Ferland, G.J. 1993, ApJ, 418, 11

Hamann, F. & Ferland, G.J. 1999, ARA&A, 37, 487

Hill, G.J., Thompson, K.L., & Elston, R. 1993, *ApJ*, 414, L1

Horne, K. 1986, *PASP*, 98, 609

Iben, I. & Tutukov, A.V. 1984, *ApJS*, 54, 335

Isaak, K.G., McMahon, R.G., Hils, R.E., & Withington, S. 1994, *MNRAS*, 269, L28

Iwamuro, F., et al. 2002, *ApJ*, 565, 63

Joly, M. 1987, *A&A*, 184, 33

Kauffmann, G. & Haehnelt, M.G. 2000, *MNRAS*, 311, 576

Kawara, K., Murayama, T., Taniguchi, Y., & Ari moto, N. 1996, *ApJ*, 470, L85

Korista, K.T., Hamann, F., Ferguson, J., & Fer land, G.J. 1996, *ApJ*, 461, 641

Kormendy, J. & Richstone, D. 1995, *ARA&A*, 33, 581

Kukula, M.J., et al. 2001, *MNRAS*, 326, 1533

Kurucz, R.L. 1992, in *The Stellar Populations of Galaxies*, IAU Symp. # 149, eds. B. Barbuy, A. Renzini, Kluwer Dordrecht, p.225

Lanzetta, K.M., Yahata, N., Pascarelle, S., Chen, H.-W., Fernandez-Soto, A. 2002, *ApJ*, 570, 492

Laor, A., Bahcall, J.N., Jannuzi, B.T., Schneider, D.P., & Green, R.F. 1995, *ApJS*, 99, 1

Laor, A., Jannuzi, B.T., Green, R.F., & Boroson, T.A. 1997, *ApJ*, 489, 656

Lilly, S.J., Le Fèvre, O., Hammer, F., & Cramp ton, D. 1996, *ApJ*, 460, L1

Mathur, S. 2000, *MNRAS*, 314, L17

Matteucci, F. & Greggio, L. 1986, *A&A*, 154, 279

Matteucci, F. & Padovani, P. 1993, *ApJ*, 419, 485

Matteucci, F. 1994, *A&A*, 288, 47

Matteucci, F. & Recchi, S. 2001, *ApJ*, 558, 351

McIntosh, D.H., Rieke, M.J., Rix, H.-W., Foltz, C.B., & Weymann, R.J. 1999, *ApJ*, 514, 40

Merritt, D. & Ferrarese, L. 2001, *ApJ*, 547, 140

Murayama, T., Taniguchi, Y., Evans, A.S., et al. 1998, *AJ*, 115, 2237

Murayama, T., Taniguchi, Y., Evans, A.S., et al. 1999, *AJ*, 117, 1645

Netzer, H. & Laor, A. 1993, *ApJ*, 404, L51

Netzer, H., Wamsteker, W., Wills, B.J., & Wills, D. 1985, *ApJ*, 292, 143

Netzer, H. & Wills, B.J. 1983, *ApJ*, 275, 445

Netzer, H., Laor, A., & Gondhalekar, P.M. 1992, *MNRAS*, 254, 15

Nolan, L.A., et al. 2001, *MNRAS*, 323, 308

Ohta, K., Yamada, T., Nakanishi, K., Kohno, K., Akiyama, M., & Kawabe, R. 1996, *Nature*, 382, 426

Omont, A., Petitjean, P., Guilloteau, S., McMahon, R.G., Solomon, P.M., & Pecontal, E. 1996, *Nature*, 382, 428

Omont, A., Cox, P., Bertoldi, F., McMahon, R.G., Carilli, C.L., & Isaak, K.G. 2001, *A&A*, 374, 371

Onken, C.A. & Peterson, B.M. 2002, *ApJ*, 572, 746

Osmer, P.S. & Shields, J.C. 1999, in 'Quasars and Cosmology', ASP Conf.Ser. 162, eds. G. Ferland & J.A. Baldwin, p.235

Papadopoulos, P.P., et al. 2000, *ApJ*, 528, 626

Perryman, M.A.C., Lindegren, L., Kovalevsky, J., et al. 1997, *A&A*, 323, L49

Peterson, B.M. & Wandel, A. 1999, *ApJ*, 521, L95

Peterson, B.M. & Wandel, A. 2000, *ApJ*, 540, L13

Pettini, M. 1999, in Proc.of ESO Workshop 'Chemical Evolution from Zero to High Redshift', ed. J. Walsh & M. Rosa, p.233

Pogge, R.W. 2000, *New Astronomy Reviews*, 44, 381

Romano, D., Silva, L., Matteucci, F., & Danese, L. 2000, *MNRAS*, 334, 444

Sanders, D.B., Phinney, E.S., Neugebauer, G., Soifer, B.T., & Matthews, K. 1989, *ApJ*, 347, 29

Schneider, D.P., Schmidt, M., & Gunn, J.E. 1989, *AJ*, 98, 1951

Shang, Z., et al. 2003, *ApJ*, 586, 52

Sigut, T.A.A. & Pradhan, A.K. 1998, *ApJ*, 499, L139

Sigut, T.A.A. & Pradhan, A.K. 2003, *ApJS*, 145, 15

Smecker-Hane, T.A., & Wyse, R.F.G. 1992, *AJ*, 103, 1621

Steidel, C.C., Adelberger, K.L., Giavalisco, M., Dickinson, M., & Pettini, M. 1999, *ApJ*, 519, 1

Storey, P.J. & Hummer, D.G. 1995, *MNRAS*, 272, 41

Taniguchi, Y., Murayama, T., Kawara, K., & Arimoto, N. 1997, *PASJ*, 49, 419

Thompson, K.L., Hill, G.J., & Elston, R. 1999, *ApJ*, 515, 487

Tinsley, B.M. 1979, *ApJ*, 229, 1046

Tremaine, S., et al. 2002, *ApJ*, 574, 740

Tresse, L. & Maddox, S.J. 1998, *ApJ*, 495, 691

van Breugel, W.J.M., Stanford, S.A., Spinrad, H., Stern, D., & Graham, J.R. 1998, *ApJ*, 502, 614

Verner, E.M., Verner D.A., Korista, K.T., et al. 1999, *ApJS*, 120, 101

Vestergaard, M. & Wilkes, B.J. 2001, *ApJS*, 134, 1

Wampler, E.J. & Oke, J.B. 1967, *ApJ*, 148, 695

Wandel, A. 1999, *ApJ*, 527, 649

Warner, C., et al. 2002, *ApJ*, 567, 68

Weymann, R.J., Morris, S.L., Foltz, C.B., & Hewett, P.C. 1991, *ApJ*, 373, 23

Wheeler, J.C., Sneden, C., & Truran, J.W. 1989, *ARA&A*, 27, 279

Willott, C.J., Rawlings, S., & Jarvis, M.J. 2000, *MNRAS*, 313, 237

Wills, B.J., Netzer, H., Uomoto, A.K., & Wills, D. 1980, *ApJ*, 237, 319

Wills, B.J., Netzer, H., & Wills, D. 1985, *ApJ*, 288, 94

Yoshii, Y., Tsujimoto, T., & Nomoto, K. 1996, *ApJ*, 462, 266

Yoshii, Y., Tsujimoto, T., & Kawara, K. 1998, *ApJ*, 507, L113

Fig. 1.— The restframe quasar spectra together with results of the multi-component analysis are shown for BRI 0019–1522, BR 0103+0032, PSSJ 0248+1802, PC 1158+4635, Q 2050–358, and BRI 2237–0607. In the top panel the quasar spectrum is shown together with the power law continuum fit (dotted line), the scaled and broadened Fe-emission template, the scaled Balmer continuum emission, and the Gaussian components to fit the  $\text{Mg II}\lambda 2798$  emission line profiles. The resulting fit is over plotted as a thick solid line. In the bottom panel the quasar spectrum is shown after subtraction of these components.

Fig. 2.— The spectrum of SDSS 1204–0021, observed in the H-band spectral region, transformed to the restframe (top panel). In the middle panel the mean  $z \simeq 4.5$  quasar spectrum is shown, scaled to match the overall spectral shape of SDSS 1204–0021 and the resulting difference spectrum is plotted in the bottom panel.

Fig. 3.— The  $\text{Fe II}/\text{Mg II}$  line ratio of the  $z \simeq 4.5$  quasars in comparison with quasars at  $z \simeq 3.4$  which have been observed previously (Dietrich et al. 2002a) are plotted as filled diamonds as a function of redshift. The  $\text{Fe II}/\text{Mg II}$  ratio of composite spectra (filled boxes, redshift sample) and comparable luminosity like the individual high-redshift quasars are displayed to illustrate the lack of evolution of the  $\text{Fe II}/\text{Mg II}$  line ratio.

Fig. 4.— The same as Figure 3 but the  $\text{Fe II}/\text{Mg II}$  ratios of the individual high-redshift quasars (filled diamonds) and composite spectra with increasing luminosity (filled boxes, luminosity sample) are plotted as a function of intrinsic continuum luminosity,  $\lambda L_\lambda(1450\text{\AA})$ .

Fig. 5.— The same as Figure 3 but the  $\text{Fe II}/\text{Mg II}$  ratios of the  $z = 3.4$  and  $z = 4.5$  high-redshift quasars (filled diamonds  $\blacklozenge$ ) and redshift sample quasar spectra (filled boxes  $\blacksquare$ ) of our study are compared to the results of Wills et al. (1985)  $\square$ , Thompson et al. (1999)  $\ast$ , Iwamuro et al. (2002)  $(\diamond, \Delta)$ , and Freudling et al. (2003) (small  $\square$ ).

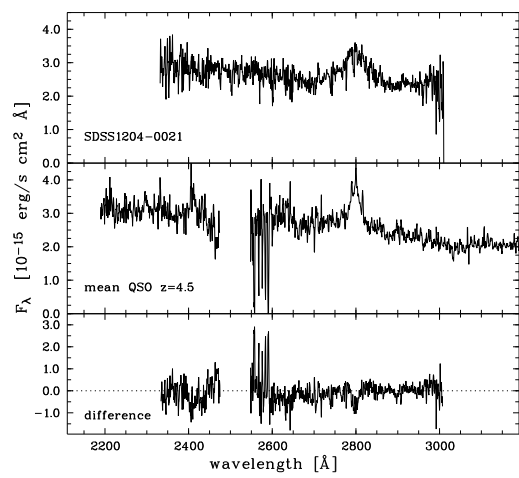
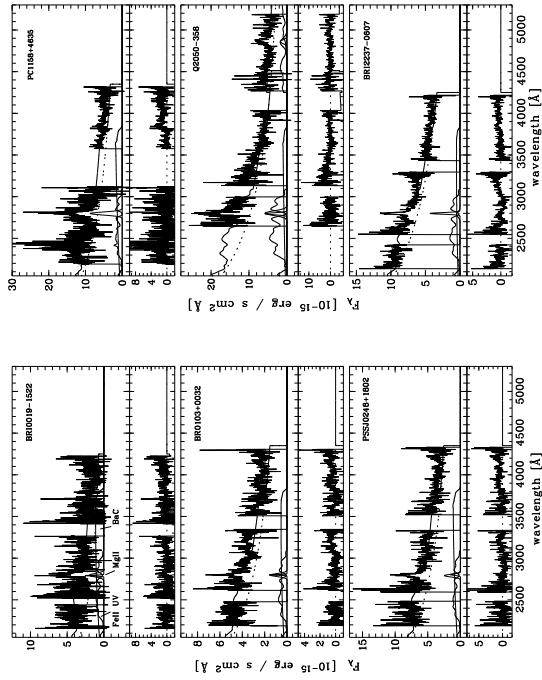
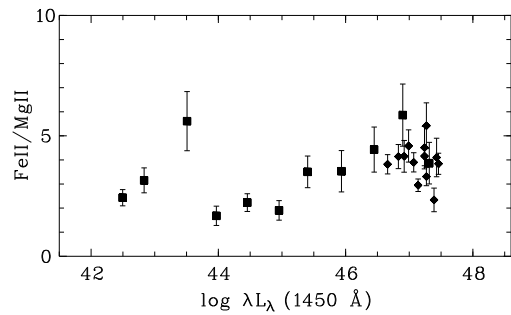
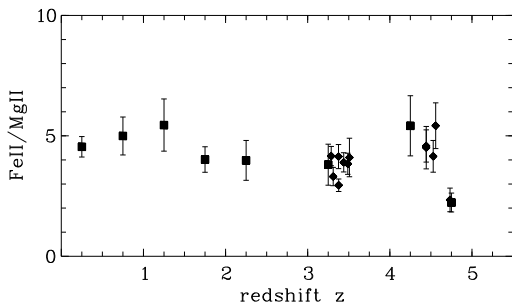


TABLE 1  
THE HIGH REDSHIFT QUASARS SAMPLE

quasar	site	date	exposure time		
			J	H	K
			[sec]		
BRI 0019-1522	CTIO	16-Sep-00	2100	2100	2100
BRI 0103+0032	CTIO	16,17-Sep-00	8700	8700	8700
PSS J0248+1802	CTIO	17-Sep-00	7200	7200	7200
PC 1158+4635	Keck	20-May-00	2400	2800	1920
SDSS 1204-0021	VLT	11-Apr-01	...	1800	...
		14-Jun-01	...	1800	...
Q 2050-359	CTIO	17-Sep-00	5700	5700	5700
BRI 2237-0607	CTIO	15,16,17-Sep-00	15800	15800	15800



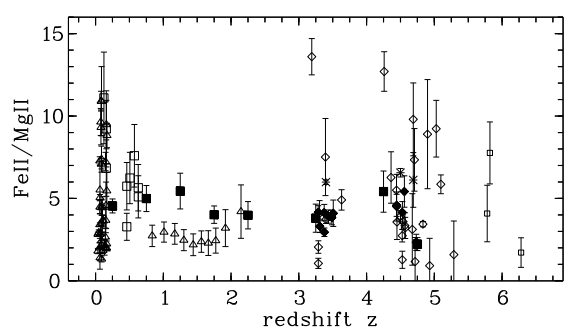


TABLE 2

Mg II $\lambda$ 2798 AND Fe II EMISSION LINE FLUX MEASUREMENTS OF THE  $z = 3.4$ ,  $z = 4.5$  QUASAR SAMPLES AND OF THE REDSHIFT AND LUMINOSITY SAMPLES.

quasar	$z$	$\log \lambda L_\lambda(1450\text{\AA})$ [ $\text{erg s}^{-1}$ ]	$F(\text{Mg II})^a$	UV Fe II/Mg II
The $z=3.4$ Sample				
Q 0103-260	3.375	46.83	$73.6 \pm 3.5$	$4.14 \pm 0.50$
Q 0105-2634	3.488	47.46	$267.4 \pm 11$	$3.84 \pm 0.44$
Q 0256-0000	3.377	47.14	$200.7 \pm 7$	$2.95 \pm 0.26$
Q 0302-0019	3.286	47.24	$341.5 \pm 10$	$4.16 \pm 0.40$
Q 2050-359	3.508	47.43	$566.5 \pm 70$	$4.10 \pm 0.80$
Q 2227-3928	3.438	47.07	$156.0 \pm 5$	$3.90 \pm 0.40$
Q 2348-4025	3.310	47.27	$155.6 \pm 10$	$3.31 \pm 0.38$
The $z=4.5$ Sample				
BRI 0019-1522	4.528	46.92	$135.9 \pm 15$	$4.15 \pm 0.66$
BR 0103+0032	4.443	46.99	$85.0 \pm 8$	$4.58 \pm 0.67$
PSSJ 0248+1802	4.443	47.24	$134.3 \pm 13$	$4.51 \pm 0.88$
PC 1158+4635	4.733	47.39	$394.8 \pm 40$	$2.34 \pm 0.49$
BRI 2237-0607	4.558	47.27	$138.5 \pm 14$	$5.42 \pm 0.95$
The Luminosity Sample				
comp.L40l	0.003	42.50	$1003 \pm 75$	$2.43 \pm 0.34$
comp.L40h	0.034	43.51	$263 \pm 10$	$5.61 \pm 1.23$
comp.L41l	0.051	43.97	$273 \pm 13$	$1.68 \pm 0.40$
comp.L41h	0.088	44.46	$258 \pm 9$	$2.23 \pm 0.37$
comp.L42l	0.267	44.95	$105 \pm 3$	$1.91 \pm 0.41$
comp.L42h	0.721	45.40	$38 \pm 2$	$3.51 \pm 0.66$
comp.L43l	1.349	45.94	$60 \pm 2$	$3.53 \pm 0.86$
comp.L43h	2.069	46.45	$81 \pm 3$	$4.43 \pm 0.94$
comp.L44l	2.780	46.90	$131 \pm 4$	$5.86 \pm 1.29$
comp.L44h	2.909	47.32	$312 \pm 21$	$3.87 \pm 0.86$
The Redshift Sample				
comp.red025	0.24	46.29	$1278 \pm 36$	$4.54 \pm 0.43$
comp.red075	0.80	46.43	$249 \pm 6$	$4.99 \pm 0.79$
comp.red125	1.28	46.56	$203 \pm 6$	$5.45 \pm 1.08$
comp.red175	1.87	46.66	$154 \pm 3$	$4.02 \pm 0.53$
comp.red225	2.14	46.70	$122 \pm 7$	$3.98 \pm 0.83$
comp.red275	2.79	46.73	...	...
comp.red325	3.17	46.74	$72 \pm 5$	$3.80 \pm 0.85$
comp.red375	3.84	46.82	...	...
comp.red425	4.26	46.76	$64 \pm 5$	$5.42 \pm 1.25$
comp.red475	4.79	46.65	$77 \pm 8$	$2.23 \pm 0.39$

<sup>a</sup> $[10^{-15} \text{ erg s}^{-1} \text{ cm}^{-2}]$